MSc Thesis

Focusing waves on skin surface to provide localized vibrotactile feedback

Valerie de Vlam
4374606

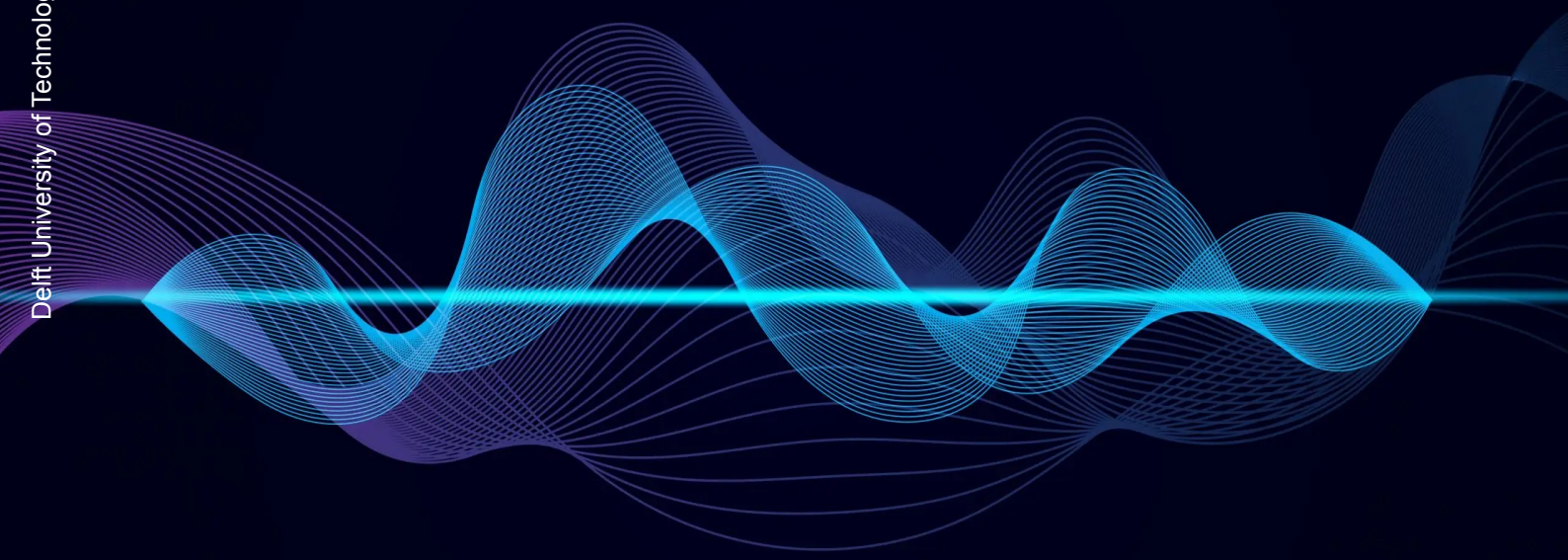

Delft University of Technology

TU Delft

Department of Cognitive Robotics

Focusing waves on skin surface to provide localized vibrotactile feedback

MSc Thesis

by

Valerie de Vlam

to obtain the degree of Master of Science
at the Delft University of Technology,
to be defended publicly on Thursday June 2nd, 2022 at 9:00.

Student number:	4374606	
Master:	Mechanical Engineering	
Track:	BioMechanical Design, Haptic Interfaces	
Project duration:	June 4, 2021 - June 2, 2022	
Thesis committee:	Dr. M. Wiertlewski,	TU Delft, supervisor
	Dr. Y. Vardar,	TU Delft, supervisor
	Dr. R. Fenton Friesen,	Texas A&M University, supervisor
	Dr. D. Dodou,	TU Delft, external member

An electronic version of this thesis is available at http://repository.tudelft.nl/.

Cover Image source (https://www.shutterstock.com/image-vector/soundwave-vector-abstract-background-music-radio-1505500757).

TU Delft

Preface

Dear reader,

I am proud to introduce to you my final master thesis. If you had told me many years ago that I would do my graduation thesis in Mechanical Engineering at the TU Delft, I probably would not have believed you. However, I am proud to say that I managed to do it and that I enjoyed it. Although, this journey would not have been possible without the uncountable people who helped me get through it.

Michael, I am grateful for being a graduate student under your supervision. I very much enjoyed the master meetings that you hosted, they established a “togetherness” spirit in the group and helped us to lift each other up. Furthermore, the sessions at your office always motivated me to keep learning and to be more curious about the “how and why” questions.

Yasemin, the weekly meetings with you were a constant platform for ideation, brainstorming, questioning, and reflecting. I really enjoyed them, as there was room to also talk about the “non-thesis” matters. I admire you for creating your own lab and I would like to apologise for all the moments we made a mess of it. Furthermore, it was so fun to see how excited you are about your own work and the work of the HITLab group members, and I feel honoured and inspired to have been a part of that.

Becca, although you now live on the other side of the world, it was so nice to be able to interact with you so many times at the start of my thesis and throughout my entire literature review. You were always there to think along and answer all my questions. Furthermore, thanks for teaching me how to be a hardware geek, and to be patient while debugging, which I know is not my best quality.

Then, there are a few people that deserve a shout-out for keeping me company at the university this year. Tammo, Felix and Luka, thanks for the many discussions in the lab and for always helping me move forward with sharing new ideas. To all the members of the Haptic Interface Technology Lab and Tactile Machines Lab, I will miss our coffee breaks and our conversations about haptics. Tijn, Mike and Belle, it always really helped to share our thesis frustrations at 3mE together. Moreover, I would like to express my gratitude to all the participants, who took time to be a part of this research.

Lastly, I could not have done this without the love and support from my family and friends. First, I want to thank my boyfriend, Marcel. Throughout the past years, he has been a steady factor in my life, helping me to structure my thoughts and always making me laugh when I needed it. I am grateful for the support of my parents throughout my entire studies. The ever-recurring motto “you cannot do any better than your best” is one that I will cherish, Pap. Furthermore, I want to thank my roommates and friends, for giving me the right distraction when I needed it but also for enduring my many replies: “sorry I cannot meet, as I a am busy with my thesis”. The last thanks go out to my left forearm which endured more than a thousand vibrations over the past year. All in all, a year of good vibrations!

Valerie de Vlam
Delft, May 2022

Contents

1

Paper

Focusing waves on skin surface to provide localized vibrotactile feedback

For obtaining the degree of Master of Science in Mechanical Engineering

Thursday 2nd June, 2022

Valerie de Vlam (4374606), Delft University of Technology

***Abstract*— Vibrotactile wearable devices are a non-intrusive and inexpensive means to provide haptic feedback directly on the user's skin. These devices utilize one or multiple vibrotactile actuators to generate vibrations across the skin and into the tissue. Combining these vibrations in amplitude can create the illusion of a funneled sensation on the skin at another location than at the actual sites of stimulation. This allows for the placement of virtual actuators on the skin, such that fewer actuators need to be deployed. However, the illusion does not take into account that the waves originating from the actuator attenuate and disperse due to the viscoelastic properties of the skin. We hypothesize that this diffusion of the elastic energy in the skin is affecting the perception of this illusion. Therefore, if we correct for the wave propagation speed, and temporally focus the stimulation, we hypothesized that the specificity of the stimulation on the skin could be drastically improved. In this paper, a novel technique, which is named the inverse filter technique, was introduced that enables to focus the amplitude, frequency and phase of vibrations to one location while cancelling them at the remaining nearby positions. We developed a wearable device for the volar surface of the forearm on which we could independently control arbitrary waveforms at any position between a set of four physical actuators. A human-subject study found that the performance in terms of localization confidence was improved significantly, whereas the precision and accuracy of the task did not improve compared to when we did not correct for the wave attenuation and dispersion. These results show that focusing waves towards a target location has a direct influence on our confidence of localizing vibrotactile stimuli on the arm. Therefore, we anticipate that our findings can benefit industries interested in including localized vibrotactile feedback on the human body surface.**

***Index Terms*—human-machine interaction, vibrotactile feedback, surface wave propagation, perceptual localization**

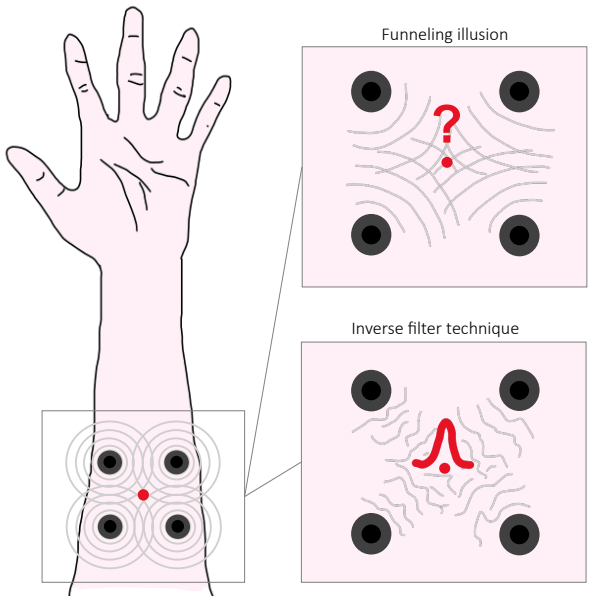

Fig. 1. Visualization of the working principles of the two rendering techniques. Left: Four vibrotactile actuators (in black) propagate surface waves across the skin (in grey). Top right: shows the principle for the funneling illusion. When all actuators send the same amplitude, frequency, and phase signal, a funneled sensation is obtained in the middle (red dot). Although, from the literature, it is unknown what kind of wave signal is retrieved at the red dot. Bottom right: represents the working principle of the inverse filter technique. This method tries to optimize the phase, frequency and amplitude of the driving signals of the actuators to create a localized haptic feedback signal between the physical actuators.

I. Introduction

Recent advances in the field of human-robot interaction, telerobotics, and virtual reality have revealed that introducing the haptic feedback modality to these disciplines has the power to significantly expand their application range and improve user experience [1]. Human skin in particular has been considered as an additional means of presenting information through the use of wearable haptic displays. Such a display is shaped by its ability to present spatial cues about an event occurring in the external or virtual environment onto the human body surface, using vibrations [2]. These vibrations are mostly generated by vibrotactile actuators that propagate vibrations across the skin surface. Through the interaction of multiple actuators, complex information can be conveyed to different body surfaces of the user [3]. Although the hand is favoured due to its high density of mechanoreceptors [4], researchers prefer to exploit other body parts because the hand is regularly used for dexterous interaction with the environment. An example in which multiple actuators work together to send vibrotactile feedback to the forearm is a phonemic-based display for speech communication. Through the use of 24 actuators on the forearm, Reed et al. were able to produce 39 different phonemic-based tactile codes to deaf-blind individuals [5]. A second example is a waistband that provides navigation advice for a soldier in unknown terrain via 8 vibrotactile actuators [6]. For these examples, where

the more typical channels of audition and sight are absent, compromised, or overburdened, vibrotactile feedback proved to be of essential value. Since these wearable displays have been developed for a variety of purposes, they take on many different forms and shapes. Nevertheless, these devices should always have a few things in common. Firstly, the stimuli on the skin should be perceived in such a way that the user can accurately and precisely localize the feedback [7]. Secondly, the wearable should be lightweight and sophisticated for the user and thus contain as few actuators as possible, as they mostly come in bulky sizes [3].

By exploiting vibrotactile illusions, researchers were able to reduce the number of actuators and thus increase the spatial resolution of the device [8] [9] [10]. These psychophysical illusions emerge when the physical stimulus applied to the human body does not accord with the perceived stimulus [11]. Thus, during a vibrotactile illusion, the stimulus is perceived at another location than at the actual site of stimulation. This allows for the placement of virtual static or dynamic actuators on the skin, such that fewer actuators need to be used. Apart from deploying vibrotactile illusions in vibrotactile devices, there is another crucial reason why to study these illusions. Namely, the existence of an illusion enables researchers to understand the working mechanisms sub-serving the perception of haptic sensations. From studying vibrotactile illusions, we gain insight into the nature of the cognitive processes that humans use to perceive the world around them.

A well-known static vibrotactile illusion that has been exploited in wearable devices is the funneling illusion (FI). In 1959, von Békésy found that when two vibrotactile actuators were simultaneously actuated on a line on the skin, with the same amplitude, frequency and phase, an illusory single focal vibrating actuator was sensed exactly in the middle between both actuators [12]. The subject experiencing the illusion would report as if "the tactile inputs are 'funneled' to a central location at which the stimulus is perceived as being more intense than at the individual sites of stimulation" [13]. By altering the amplitude of the physical actuators, the perceived location of the virtual actuator varies. This illusion is also known as the 'mislocalization illusion'. Yet researchers have taken benefit from applying the illusion since now a virtual actuator can be created anywhere between a set of physical actuators.

Although it seems that utilizing vibrotactile illusions only comes with advantages, in practice it turns out to be challenging for users to accurately localize the static stimuli originating from an illusion. Barghout et al. experimented with the funneling illusion on the forearm and found that the average detection rate for localizing the illusion midway between the two actuators, with an inter-tactor spacing of 40 mm, was 12% [1]. These results improved with a factor of 2 as the illusion moved closer to one of the two physical actuators.

A possible cause for the deficient results could be deduced from studying the wave mechanics on the skin. It has long been observed that locally applied vibrations evoke mechanical waves distributed on the skin surface [14]. Through mathematical modelling, Andrews et al. found that surface waves dominate after vibrotactile stimulation. They cooperatively travel through all layers of skin and across the skin surface [15]. As our skin is viscoelastic, surface waves in such tissue are attenuated and dispersed, yielding frequency-dependent damping $\delta(f)$ and wave speeds $c(f)$. Dandu et al. found that the low-frequency waves have slower decay rates and move with lower speeds across the skin compared to the high-frequency content [16]. These results suggest that in terms of wave speed the low-frequency content will always lag behind the high-frequency content, such that the surface waves cannot reach the location of the funneling illusion at the same moment in space and time. Moreover, waves get attenuated over the distance travelled. To quantify this decay, Sofia and Jones assessed that approximately 80% of the amplitude of the surface wave is reduced at a distance of 8 mm from the source of actuation [2]. Subsequently, we hypothesize that due to wave attenuation and dispersion, the measured wave signal at the virtual actuator of the funneling illusion cannot be spatially summed into a focused wave. We speculate that this is the reason why the poor localization results were obtained. Moreover, it was discovered that when multiple vibrotactile actuators in close contact are simultaneously vibrating the body surface, they will not only recruit the mechanoreceptors at the actuators site but also a large population of mechanoreceptors with receptive fields even up to 60 mm [17]. As our tactile localization is dependent on mechanoreceptor depolarization [18], this may also make it difficult for humans to exactly pinpoint where the vibration is localized [19]. Thus, for successful vibrotactile localization, we hypothesize that we need to focus the waves at the surface of the skin.

Our objective is to develop a rendering method that, in contrast to the funneling illusion, can incorporate the frequency-dependent attenuation and dispersion on the skin to manipulate the time of arrival of the surface waves at the target location. This way, we aim to generate localized vibrotactile feedback at any position between a set of physical actuators, by focusing the amplitude, frequency and phase of the surface waves to one point while cancelling them at the remaining positions on the skin. As a result, we predict to recruit a smaller population of mechanoreceptors and anticipate that our localization performance should be increased.

Recently, the inverse filter technique (IFT) has been proposed to control the propagation of vibrations on a tactile screen [20]. The screen contained a finite number of actuators glued to the bottom side of the glass plate. Through the independent control of the frequency, amplitude and phase of the actuators, arbitrary waveforms at any position on the plate, and not only on the actuators, could be produced. This way, a user could place multiple fingers on the screen and yet feel different types of stimuli at each finger [21]. Pantera and Hudin showed that they could control the target displacement at one finger with a burst at 250 Hz, 25 cycles and amplitude of 1 μm, while a second and third finger, located very close to the first finger on the screen, perceived

zero displacement. We aim to deploy the same technique to the skin surface and verify if we can create the scenario described above. Yet, instead of taking the fingers as reference points, different locations on the skin between the actuators are the control points. The two working principles of the funneling illusion and inverse filter technique are visualized in Figure 1. The inverse filter technique is similar to the funneling illusion, in the sense that both render "virtual" vibrations anywhere between the physical actuators. However, the working principles for both methods differ. They will be explicitly explained in the next chapter.

A. Research Objective

The aim of this thesis is two-fold. First, it aims to show whether the inverse filter technique can be implemented on the skin surface, such that the amplitude, frequency and phase of the surface waves originating from the actuators are focused to one point in space, while cancelled at the remaining positions. Second, a human subject study is conducted to test the localization performance for both inverse filter technique and funneling illusion. This study examines whether our performance is sensitive to the focusing of surface waves and subsequently whether our localization ability is improved in terms of precision, accuracy and confidence.

B. Outline

Section II explains the theory of the two different types of rendering techniques used. Section III presents the newly developed wearable device and shows the design of the stimuli. Section IV zooms into the skin mechanics and shows whether the inverse filter technique can be implemented on the skin to generate localized vibrotactile feedback. The procedure and results of the perceptual experiments are presented in the subsequent section. Finally, the results are discussed, conclusions are drawn and limitations of the study are appointed in section VI.

II. Background

A. Inverse filter technique

The method used to control the propagation of vibrations across the skin is called the inverse filter technique [20]. Before its application in haptics, the method was applied in the medical imaging [22] and audio rendering domain [23] [24]. The following equation captures the relationship between a signal $s_q(t)$ driving the actuator q and the displacement $u_c(t)$ at a control point c on the skin [25]:

$$u_c(t) = h_{cq}(t) \otimes s_q(t) \tag{1}$$

Here $\otimes$ is a convolution operator and $h_{cq}(t)$ is the impulse response between actuator q and control point c. In the frequency domain, this equation is written as follows:

$$U_c(\omega) = H_{cq}(\omega) S_q(\omega) \tag{2}$$

Where ω is the angular frequency and H_{cq} is the transfer function of the skin between one actuator and one control point. However, in our case, we consider multiple actuators and multiple control points on the surface. Therefore, the previous formula must be expanded. In this paper we assume the skin to be linear, such that the superposition principle holds. This implies that the displacement at a single control point is equal to the addition of the separate actuators and that the output at a control point is homogeneous. In the end, this leads to the following matrix form:

$$\begin{pmatrix} U_1 \\ U_2 \\ \vdots \\ U_c \end{pmatrix} = \begin{pmatrix} H_{1,1} & H_{1,2} & \cdots & H_{1,q} \\ H_{2,1} & H_{2,2} & \cdots & H_{2,q} \\ \vdots & \vdots & \ddots & \vdots \\ H_{c,1} & H_{c,2} & \cdots & H_{c,q} \end{pmatrix} \begin{pmatrix} S_1 \\ S_2 \\ \vdots \\ S_q \end{pmatrix} \tag{3}$$

In condensed form this is written as $U(\omega) = H(\omega)S(\omega)$. The concept of inverse filtering is to inverse, for each frequency component, the $H(\omega)$ matrix, to calculate the driving signals $S(\omega)$ that will produce the target displacements $U(\omega)$ at the set of control points. Here, $H(\omega)$ is obtained from a calibration step and the signal $U(\omega)$ is defined by the displacements that we want to obtain at the different control points on the skin. Since in our case, the number of control points will be different from the number of actuators, the inverse operation can not be achieved by a classical matrix inversion, but instead is computed via a pseudo-inverse ($^+$). Then, the driving signals are calculated as follows:

$$S(\omega) = H(\omega)^+ U(\omega) \tag{4}$$

Finally, the driving signals $S(\omega)$ are transformed back into the time-domain by an inverse Fourier transform to drive the separate actuators with each their own $s_q(t)$. Figure 2a shows the mechanical working principles of the inverse filter technique on the skin for one actuator. Here, an arbitrary multi-frequency signal was desired at a single control point 16 mm spaced from the actuator. It is clear that through inverse filtering, the actuator optimizes the amplitude, phase and frequency content of the driving signal $s_q(t)$ to achieve the desired displacement at $u_c(t)$. From analyzing the frequency spectrum of the driving signal it becomes apparent that the actuator first sends a low-frequency signal, which is characterized by low speeds and low damping ratios (see detailed results in Appendix A). Subsequently, high-frequency content follows with higher speed and larger damping coefficients. Finally, the signals catch up with each other at 16 mm to create the desired wave at the control point. Even though a focused wave is obtained at 16 mm, it is clear that the maximum amplitude of the other locations exceed the one at the control point. This explains why multiple actuators and multiple control points are required to fulfill the conditions of a focused vibration at one point and minimized vibrations at the other points. To conclude, the inverse filter technique allows for the creation of localized feedback at different control points on the skin. To do so, the method

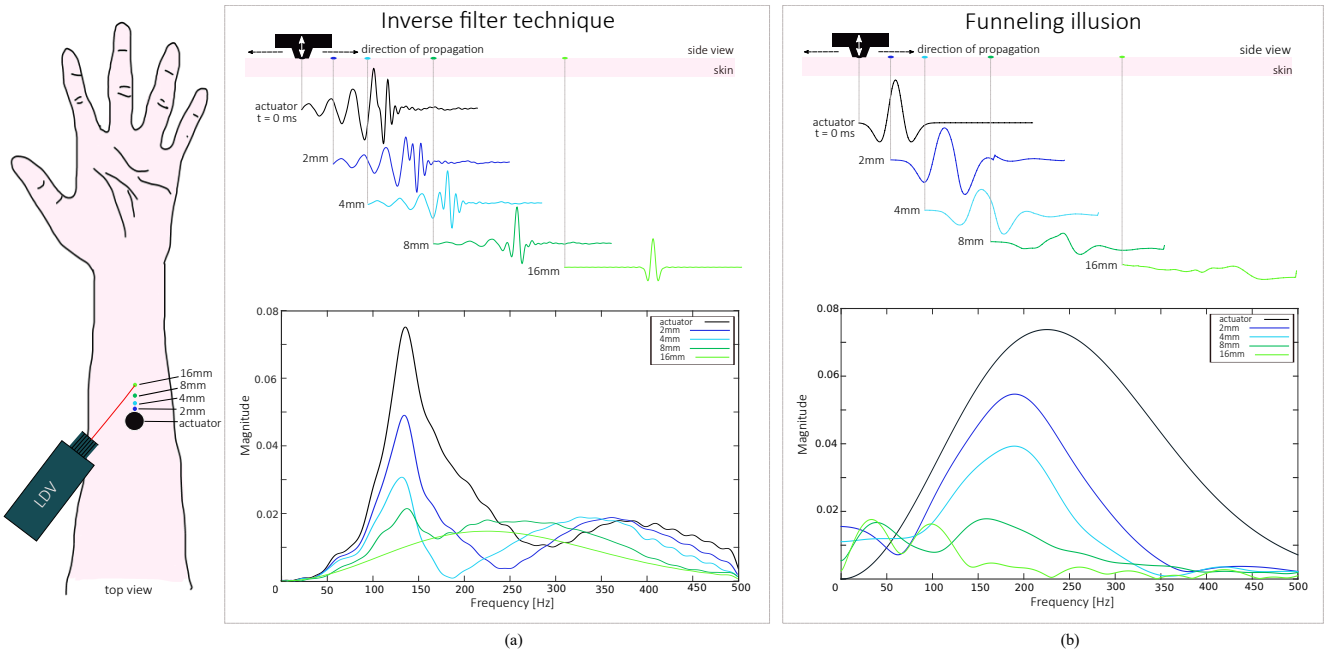

(a) (b)

Fig. 2. Visualization of how a multi-frequency signal gets attenuated and dispersed at different locations via (a) the inverse filter technique and (b) the funneling illusion. On the left, the set-up is visualized. One vibrotactile actuator is fixed to the volar surface of the left forearm and sends vibrations across the skin in all directions. A Laser Doppler Vibrometer (LDV) measures the skin displacement over time in response to the driving signal of the actuator. In total, we measured the vibration at the actuator and four different locations on the skin surface. At the top of each sub-figure (a,b) the measured skin displacements are shown over time. At the bottom the frequency spectrum of the wavelets are visualized for the measured locations.

requires the $H(\omega)$ and $U(\omega)$. The design of both signals is treated in section III-B.

B. Funneling illusion

To date, the funneling illusion allows for the placement of a virtual actuator anywhere between a set of physical actuators [13]. To obtain this virtual actuator, each physical actuator must drive with the same frequency and phase stimulus $s(t)$. The only variable that is varied between the different actuators, is the amplitude A_q. The formula for the driving signal of each physical actuator is therefore calculated as follows:

$$s_q(t) = A_q s(t) \tag{5}$$

In the past, researchers have come up with two types of psycho-physical models to define the amplitude of the physical actuators [26], namely a linear and a logarithmic rendering algorithm. Seo and Choi reported that the logarithmic approach is favoured when forecasting the intensity of the illusion, while the linear approach is preferred when predicting the location of the illusion [27]. As the aim of the experiments is to predict the location of the funnelling illusion, the linear rendering algorithm was selected. The amplitude A_q of each physical actuator is therefore computed as follows [28]:

$$A_q = A(1 - \frac{d_q^x}{D^x})(1 - \frac{d_q^y}{D^y}) \tag{6}$$

Where A is the maximum amplitude in Voltage, d_q^x and d_q^y are the horizontal and vertical distances from the actuator q to the virtual actuator location and D^x and D^y are the maximum distances between the actuators. Once the amplitude A_q for every actuator is computed, the driving signal for each actuator $s_q(t)$ can be determined. The design of $s(t)$ is treated in section III-B.

Figure 2b shows the mechanical working principle for the funneling illusion on the skin for only one actuator. At $t = 0\,ms$ a multi-frequency signal with a certain amplitude is departing from the actuator. Due to the frequency-dependent attenuation, the frequency spectrum at the bottom of the figure displays that the high-frequency content dampens out more quickly than the lower frequencies. Therefore, at 16 mm the signal only consists of low frequencies and no focused vibration is obtained at the ”virtual” actuator.

To summarize, the funnelling illusion is an already existing method for localizing vibrations on the skin and is based on only modulating the amplitude of the physical actuators. However, the method does not take into account the mechanical properties of the skin $H(\omega)$ and does not control the vibration signal that arrives at the virtual location $U(\omega)$. All these properties are incorporated in the inverse filter technique and to do so, this latter method not only modulates the amplitude of the physical actuators, but also controls the phase and frequency of the driving signals. The latter is what differentiates the two rendering methods from each other.

III. Methods

A. Apparatus

A wearable 3D-printed device allowed for the placement of a two-by-two array of vibrotactile actuators on the volar surface of the arm (see the top-right image in Figure 3). The inner diameter of the device was 22 cm and could be attached to the left forearm of the participant via two velcro straps. Force sensors (IEFSR, 19) on each strap ensured that the device was fastened with an equal amount of force. In this study, we used voice coil actuators (Tectonic, TEAX14C02-8) that vibrate through a moving magnetized coil. Their bandwidth frequency was within the human sensitivity range with a maximum peak at 580 Hz. The vertical and horizontal spacing between the centre-points of the actuators was 45 mm, which is more than twice the measured static two-point gap threshold on the forearm [29]. Modelling and experimental testing showed that the aforementioned spacing proved to be optimal in terms of amplitude control and tactile perception. To ensure that the vibrations originating from the actuators were better distributed across the surface, small closed-end cones were designed and attached to the part of the actuator that would be in direct contact with the skin [7]. This way, the total contact area between the actuators and the skin was reduced by a factor of 4. Furthermore, these cones prevented direct contact of the rest of the wearable housing with the skin and therefore prevented part of the attenuation of the generated vibrations and reduced perceptual masking [3].

Once the wearable device was attached to the arm of the participant, cutaneous vibrations were sent to each of the actuators. A computer with a pre-programmed code written in Matlab was connected to a data acquisition board (NI, cDAQ-9174) which generated the vibrations through an amplifier (MIKROE-3077) to the actuators. While the actuators were creating a vibration signal on the skin surface, non-contact measurements of the skin in response to the vibrations could be captured. The cutaneous vibrations were collected via a non-contact Laser Doppler Vibrometer (Polytec, sensor head OFV-505 and controller OFV-5000) and the DAQ allowed for a synchronous emission of actuator signals and acquisition of vibrometer signals.

B. Stimuli Design

1) Inverse filter technique: As indicated in equation 4, this technique calculates the driving signals by incorporating $H(\omega)$ and $U(\omega)$.

$H(\omega)$ is obtained from the calibration matrix $G(\omega)$. Both matrices are closely related, however, differ in their form. The calibration matrix $G(\omega)$ contained the relation between the physical actuators and the grid surface g, whereas $H(\omega)$ captured the relationship between the physical actuators and a set of control points c within the grid surface. Here, the grid surface g consisted of 9 points: 3 points along the longitudinal axis and 3 points along the transverse axis of the arm. The grid, with its corresponding numbers, is shown by the red dots in the top left in Figure 4. The horizontal and vertical

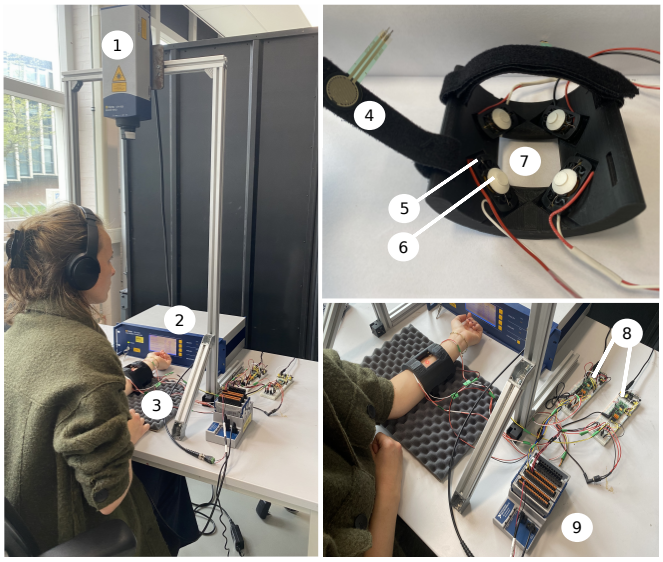

Fig. 3. Experimental setup with 1. Vibrometer sensor head, 2. Vibrometer controller, 3. Wearable device, 4. Force sensor, 5. Vibrotactile actuator, 6. Closed-end cone, 7. Hole for vibrometer measurements, 8. Amplifiers, 9. Data acquisition board.

spacing between two adjacent grid points was 1.33 cm, such that the total grid covered an area of $4 \times 4\, cm^2$ on the forearm. The procedure for measuring one entry of $G(\omega)$ is visualized at the top of Figure 4. An exponential sweep sine signal sequence of duration $T = 2s$, from $10 - 500Hz$ was sent to one of the actuators, while simultaneously the resulting skin displacement signal at a grid point was measured with the vibrometer. Afterwards, a Fourier transform was performed on both signals. The ratio of both Fourier domain signals then formed one entry in the matrix. This procedure was repeated for all actuators (4) and all grid points (9) to obtain the entire calibration matrix $G(\omega)$. The signals were sampled at F_s = 10 kHz, such that the resulting calibration matrix had a dimension of $G[9, 4, 2 \times 10^4]$. Here, $G(\omega)$ captured the mechanical activity of the actuators, as well as the dispersion and attenuation of waves from the actuators onto the skin surface [21]. It is therefore that this matrix is referred to as the skin model. Once it was determined which selection of points in the grid are controlled c (explained in the next paragraph), the corresponding rows from the calibration matrix could be selected and they formed $H(\omega)$. Thus, the resulting dimensions of $H(\omega)$ were $[c, 4, 2 \times 10^4]$, where c is the total number of control points.

The objective of the IFT was to focus the amplitude, frequency and phase content of the surface waves at one grid point (target) while cancelling all the waves at the remaining positions in the grid. This was achieved by designing the target displacements at the control points, in a way that one location in the grid followed a signal with a high amplitude over time, while the amplitude of the other control points in the grid was minimized. In this paper, the high amplitude signal was given by a Ricker wavelet. This signal was selected because

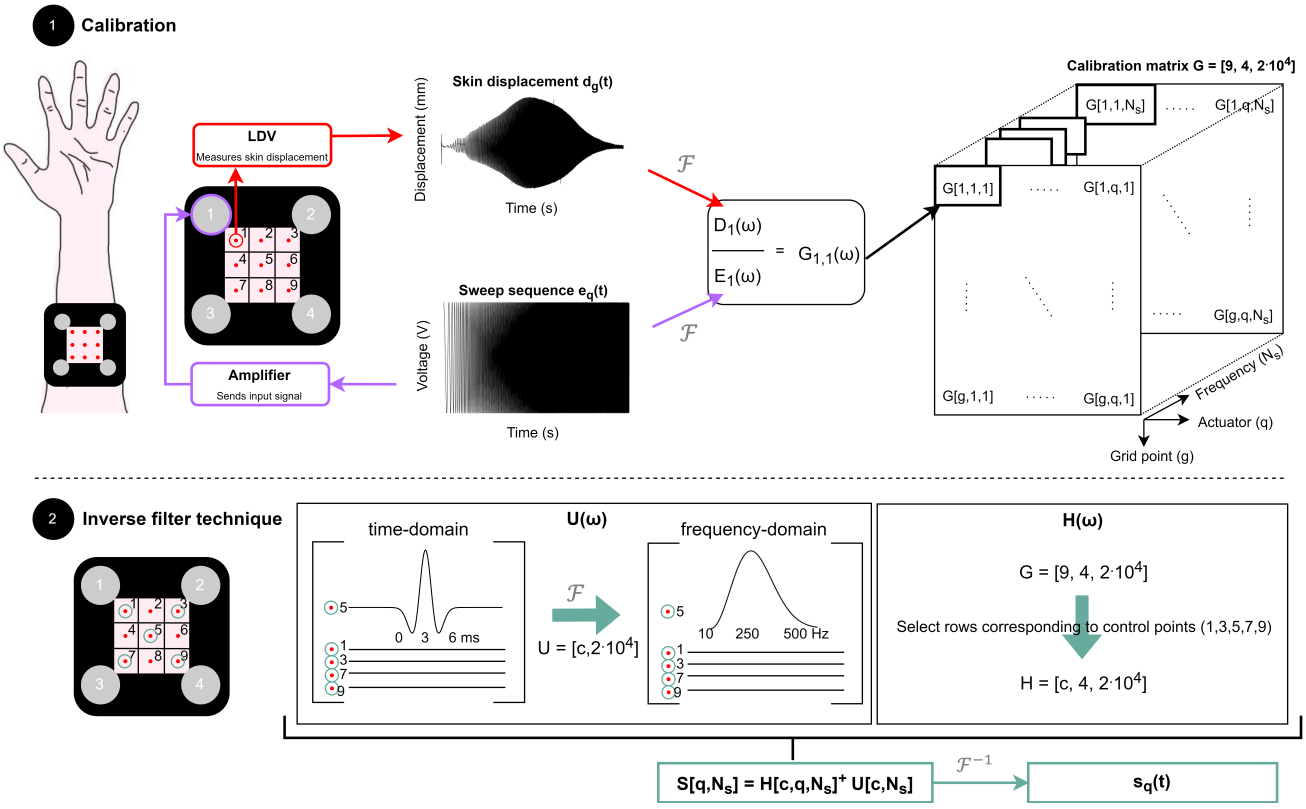

Fig. 4. Explanation of the inverse filter method. On top, the step-by-step approach is shown for how we obtained one entry in the calibration matrix $G(\omega)$. A sweep sequence is sent to actuator 1 (purple circle) and simultaneously the skin response to the actuation is measured at grid point 1 with the vibrometer (red circle). Both signals are transformed to the Fourier domain ($\mathcal{F}$) and divided by each other. This results in the transfer function $G_{1,1}(\omega)$, which forms the first entry in the matrix. Once this step is completed, the next actuator in line (2) fires the same sweep signal and the vibrometer simultaneously measures the skin displacement at the *same* grid point (1), resulting in another transfer function. The latter function will form the next entry in the matrix: $G_{1,2}(\omega)$. Eventually, this process is repeated for each actuator and for each grid point to obtain the entire G-matrix: $[9, 4, 2 \times 10^4]$. At the bottom, it is shown how the inverse filter technique works when location 5 in the grid was considered the target. This process is identical for when the other eight points in the grid are the target, yet the combination of controlled points will be different. First, the five different control points are designed in the time domain: the top signal represents the Ricker wavelet and the other four are the signals with zero displacements over time. All control signals are transformed to the Fourier domain and placed into one vector. Next, the H-matrix is formed by selecting the five rows from the calibration matrix G, corresponding to the 5 grid points that we are controlling. Once both $H(\omega)$ and $U(\omega)$ are known, the IFT calculates the four driving signals needed to obtain the displacements at the five control points via a pseudo inverse. Lastly, the driving signals are transformed back to the time domain via $\mathcal{F}^{-1}$.

it has the ability to achieve a symmetric peaked shape with a high amplitude over time. In literature, the Ricker wavelet is referred to as the Mexican hat wavelet, because it takes on the shape of a sombrero when used as a 2D image (screenshots of the time- and frequency-domain wavelets are shown at the bottom left of Fig. 4). The formula for the Ricker wavelet is captured by the following equation:

$$u_c(t) = A_c(1 - t^2)e^{-t^2/2} \tag{7}$$

Here A_c is given by the maximum amplitude in mm. When the time-domain signal is transformed to the frequency domain, the frequency content ranges between $10 - 500Hz$, which is similar to the frequency content of the calibration matrix. Furthermore, the maximum power of the Ricker wavelet was at $250Hz$. This frequency coincided with the peak sensitivity of the Pacinian Corpuscles [30], the type of mechanoreceptors that sense vibrations in the skin. Now, that the high amplitude signal was designed, the IFT needed to ensure that the other eight locations in the grid converged towards zero displacement. We found that when the remaining eight points in the grid were controlled to have zero displacement, the pseudo-operation was incapable of finding a solution for a Ricker wavelet at the target. Via experimental testing and modelling, we found that controlling only four out of the eight grids with zero displacements, resulted in a localized Ricker wavelet at the target while the amplitude at the other eight locations was minimized. For example, when a Ricker wavelet was desired at the middle point in the grid (5), we controlled the four locations at the corners with zero displacements ($u_c = 0$) (see bottom left of Fig. 4). To summarize, $U(\omega)$ is a combination of the frequency-domain Ricker wavelet and four zero displacement signals, where the Ricker wavelet forms the target location. Eventually, both $H(\omega)$ and $U(\omega)$ are substituted in equation 4 to obtain the four driving signals $s_q(t)$.

2) Funneling illusion: The funneling illusion was found via a straightforward operation. The only condition for the funneling illusion is defining the driving signals $s_q(t)$. In this paper, we used a multi-frequency signal, such that each physical actuator q simultaneously generated a Ricker wavelet of the form:

$$s_q(t) = A_q(1 - t^2)e^{-t^2/2} \tag{8}$$

Here A_q is the amplitude of the vibration in Voltage and is determined via equation 6. Furthermore, it is clear that equation 8 resembles equation 7. This was chosen intentionally, such that both methods could be compared with one another. Nonetheless, there is a crucial difference because the displacement at the target of both methods is not identical. Here, the displacement at the funneling illusion after stimulation is unknown. Yet, we managed to obtain it from the system calibration matrix $G(\omega)$. The latter will be explained in the next subsection.

3) Combination: Next to the IFT and FI method, a third rendering technique was added. This last method is a combination of the aforementioned methods, in the sense that it employs the inverse filter technique principles to calculate the driving signals of the physical actuators $s_q(t)$. However, instead of taking a Ricker wavelet as displacement $u_c(t)$ at the target, the obtained skin displacement at the "virtual" actuator from the funneling illusion is used as $u_c(t)$. Subsequently, the corresponding driving signals that are necessary to achieve the same target displacement as the funneling illusion could be calculated via the inverse filter technique. This implies that the target displacements at the location of the funneling illusion and the combination method are identical, while the driving signals differ. The driving signals for the combination method namely exploit the viscoelastic properties of the skin, while the funneling illusion does not account for this phenomenon. This way, we could verify whether manipulating the time of arrival of the waves at the target location via phase, frequency and amplitude control influenced our perception of localization, compared to when this was not done via the funneling illusion. An overview of the workflow per rendering method is seen in Figure 5.

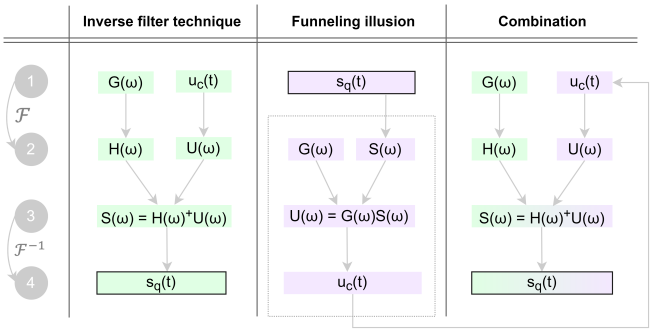

Fig. 5. Overview for how the driving signals $s_q(t)$ are obtained per rendering technique.

IV. Surface wave propagation

A. Measurement Procedure

When skin tissue is stimulated from four different sources with a certain inter-tactor spacing, surface waves will propagate and interact with each other along the skin surface. In what manner the waves are interacting with each other, was measured per rendering method and target location. The middle column of Figure 5 exhibits the workflow for how the propagation from the funneling illusion was obtained. This procedure is analogous for the other two rendering techniques. Once the driving signals of the four vibrotactile actuators were computed for a certain target location, they could be transformed to the frequency domain and multiplied with the calibration matrix $G(\omega)$. This eventually resulted in the skin displacement in mm at the nine different grid points over time. Through interpolation, the total displacement in between the grid points could also be constructed.

B. Results

Figure 6 and 7 show the results of the wave propagation on the arm of a typical participant after stimulation with the three different rendering methods. Here, Fig. 6 displays the propagation when the location in the middle of the grid was the target (5) and Fig. 7 does so for a location on the edge of the grid (6). A metric was created that captures the relation between the total amplitude over time at the target compared to the other eight non-targets in the grid. The metric is called signal strength, S, and can be calculated as follows:

$$S = \frac{A_{target}}{\frac{1}{8}\sum_{i=1}^{8} A_{non-target}} \tag{9}$$

Here, the numerator is equal to the total area under the absolute curve of the black solid line of Figure 6 and 7. Whereas, the denominator produces the average value of the areas under the absolute curves of eight black dotted lines. When $S > 1$, it means that the area under the curve of the target is larger compared to the average of the non-targets. After all, this indicates that a focused vibration was established at the target, compared to the rest of the measured skin locations. When $S < 1$, the area of the non-targets is larger than the target and no focused vibration was constructed on the body surface. The signal strength outcomes for when each separate location in the grid was considered as target, for that same participant from which the wave propagations are plotted, are found in Table I. The four locations on the edges and corners of the grid are combined into a single value, as the four locations share the same properties in the grid.

The results in Figure 6a and 7a show that, with the use of the inverse filter technique, we can focus surface waves on the arm to achieve an optimal amplitude difference between the target and the non-targets. This result can be explained through three observations. First, the signal strength values for the IFT

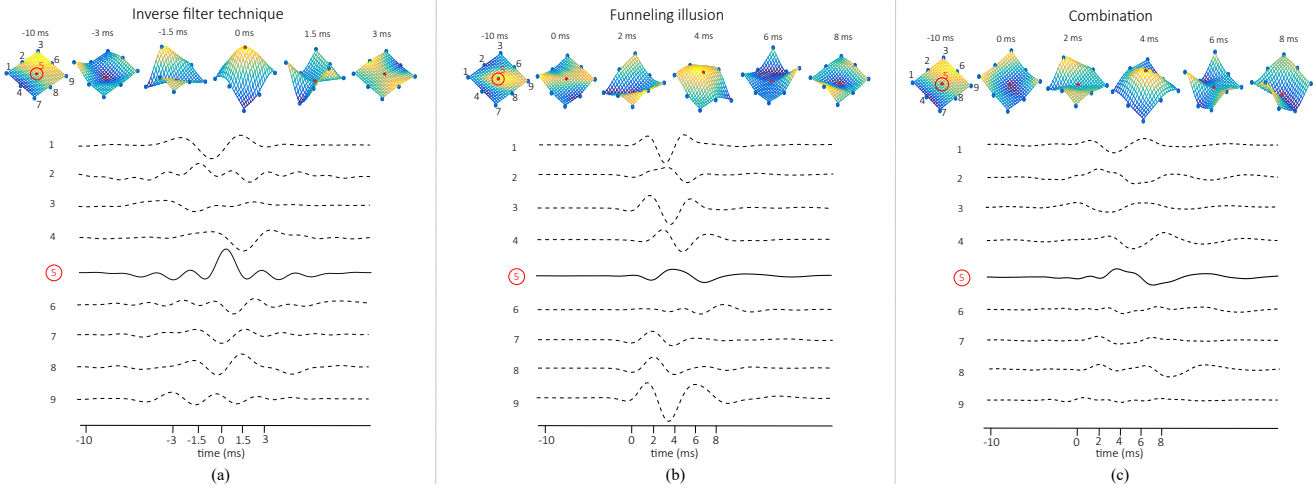

Fig. 6. Surface wave propagation results from Participant 2, for the case that location 5 is the target location. From left to right the results are plotted for (a) the inverse filter technique, (b) the funneling illusion and (c) the combination. The top part of each sub-figure shows the wave propagation in space for six key moments in time, and the bottom part displays the skin displacement for all nine different grid points over time. Here, the black solid line is the displacement of the target location, whereas the black dotted lines represent the displacements of the remaining eight grid points over time.

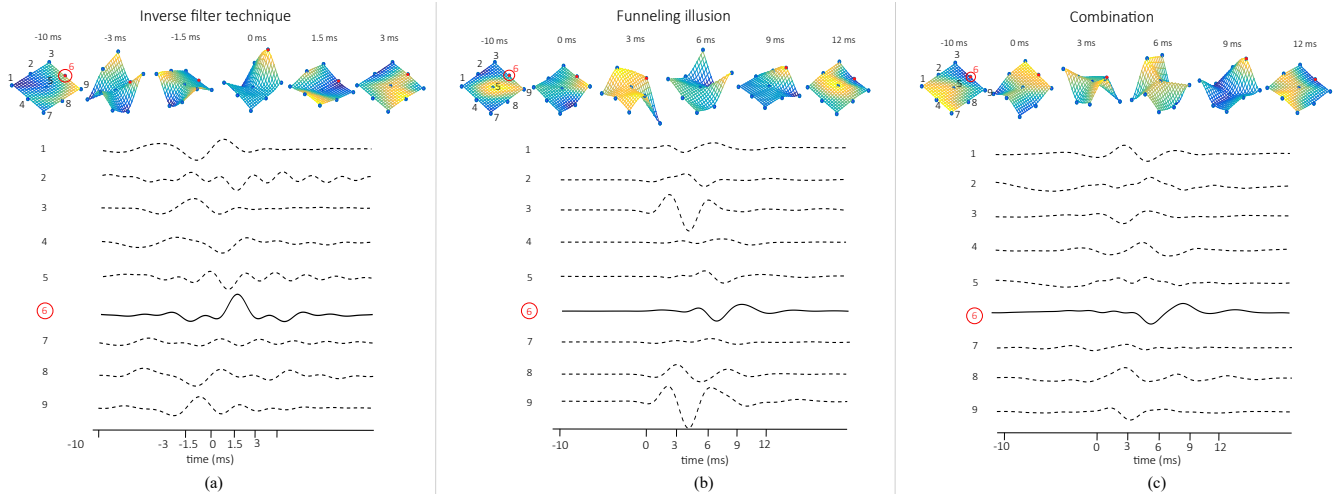

Fig. 7. Surface wave propagation results from Participant 2, for the case that location 6 is the target location.

	Inverse filter technique	**Funneling illusion**	**Combination**
Middle (5)	1.31	0.63	1.72
Edges (2/4/6/8)	1.34±0.09	0.67±0.32	1.69±0.19
Corners (1/3/7/9)	2.25±0.56	2.42±0.79	2.60±0.92

TABLE I
SIGNAL STRENGTH VALUES FOR PARTICIPANT 2. THE FOUR LOCATIONS ON THE EDGES AND CORNERS OF THE GRID ARE COMBINED INTO A SINGLE VALUE (MEAN + STANDARD DEVIATION). AS EACH VALUE IS OBTAINED THROUGH A DIVISION, THE RETRIEVED NUMBER HAS NO UNIT.

for both locations are > 1 (see left column in Table I). Second, at the time of impact, $t = 0\,ms$, the amplitude of the target location is the highest with respect to the other eight locations on the arm. This observation not only holds for the time of impact but also for $1\,ms$ before and after the impact. Third, over time the maximum amplitudes of the non-target locations in the grid never exceed the maximum amplitude of the target. The results of the wave propagation from the funneling illusion exhibit that no focused vibration was obtained at the target (check Fig. 6b and 7b), as we found signal strengths < 1 for both locations (see the middle column in Table I). From both figures, we can observe that the maximum amplitude of the target is lower compared to the maximum amplitude of the non-targets. This observation is clearly illustrated in Figure 7b. At $t = 0\,ms$, location 3 and 9 (the ones next to the physical actuators) start to displace. Due to the time-dependent wave fields, the waves reach location 6 at $t = 9\,ms$ and a funneling

illusion is obtained. It is apparent that although at $t = 9\,ms$ the amplitude of the target is highest, larger amplitudes at the actuators-side are needed to reach to the target.

The results of the wave propagation for the last type of rendering method are provided in Figure 6c and 7c. Both figures show that the displacements at the target locations are almost equivalent to the displacements at the targets from the funneling illusion. Yet, for the combination technique, the displacements at the non-target locations are minimized through the IFT principle and thus vary with respect to the ones from the funneling illusion. From both Figure 6c and 7c, it is clear that again the inverse filter technique succeeds in focusing surface waves on the arm to achieve an optimal amplitude difference between the target and the rest of the grid ($S > 1$).

To summarize, we have seen that the wave propagation differs per type of rendering method for when a location in the middle (5) and the edge (6) of the grid were the target. The wave propagations for when the other three remaining edge locations (2, 4 and 8) are the target are very similar to the propagation of Figure 7. Therefore, they are not separately visualized in this paper. Furthermore, we found that when the locations in the corners are the target, strength values of > 1 were obtained for all the different methods. This indicates that for the corner locations, we could not verify whether the difference in signal strength (< 1 and > 1) between the methods resulted in a noticeable increase in localization performance. This could only be done for the edges and middle locations. This will be analyzed in the next section.

V. Perceptual Experiments

A. Participants

20 healthy adults (9 male, 11 female) participated in the experiment. All participants were aged between 19 and 42 years (mean = 25.8, standard deviation = 4.3). No participants reported any abnormalities in their tactile or kinesthetic sensory systems. The research was approved by the TU Delft Human Research Ethics Committee (case number 1985) on the use of humans as experimental subjects.

B. Experimental Procedure

After each participant was seated at a table, the wearable device (see Figure 3) was placed on the lower left arm with the middle point of the device being aligned with the middle of the forearm. To ensure that each velcro strap was fastened with $10\,g$, force measurements were executed. Hereafter, the left arm was positioned on foam to establish a stable and comfortable pose within the field of view of the vibrometer. Then, retro-reflective tape, with the same dimensions as the grid surface, was taped onto the skin. The tape ensured that the laser light was reflected back into the vibrometer. Moreover, the nine grid points were printed on the tape, such that we knew at which locations, vibrometer samples had to be taken. Afterwards, the system calibration could commence to obtain the entire matrix $G(\omega)$ (see Fig. 4). Once this matrix was retrieved, the driving signals $s_q(t)$ for the inverse filter and the combination technique could be calculated. When all the driving signals were computed according to Fig. 5, a transparent foil was covered on top of the wearable device. On the foil, a 3×3 grid was printed containing the nine grid numbers. Participants wore noise-cancelling headphones to cancel out audio cues originating from the actuators. Once all steps were completed successfully, the official experiment could commence.

1) User study 1 - identification: User study 1 aimed to understand the perceptual identification performance of the three different rendering techniques. For that, vibrotactile stimuli were rendered on the forearm and the participants were asked to identify where in the area between the actuators they perceived the vibration. Each trial started with a brief beep via the headphones, while shortly after, a participant would receive a stimulus at a randomly-selected grid point. Then, the participant had to indicate via a numeric keypad at which of the nine grid points they perceived the rendered stimulus. This procedure was repeated three times per grid point with breaks in between. Hence, the total number of trials for user study 1 per participant was 81: respectively 3 different rendering methods × 9 different grid locations × 3 repetitions. As a result, the accuracy and precision of the identification task could be measured per target location and rendering method. Before starting with the main session, a training session was provided to each participant, which was fully identical to the main session.

2) User study 2 - confidence: User study 2 examined the confidence that participants had while localizing the vibrotactile feedback on the forearm. This study used the same hardware set-up and experimental procedure as user study 1, however now participants could select more than one grid point if they were unable to point a single grid point where they perceived the feedback. The method that showed a higher confidence, is represented by a minimum number of grid points selected.

C. Results

1) User study 1 - identification: The purpose of user study 1 was to test the subjects' ability to localize vibrotactile feedback in the 3×3 grid in terms of precision and accuracy. Figure 8 shows for each of the nine targets, the perceived sensation per rendering method for all 20 participants. The target locations are represented by the red stars and can be denoted by (x_i^t, y_i^t), where i stands for one out of the 9 locations on the 3×3 grid. The perceived locations (x_i^p, y_i^p) are displayed by 2D Gaussian distributions $N_i(\mu_i, \Sigma_i)$. Here μ_i describes the mean of the perceived location for all participants and Σ_i is the covariance matrix. The latter consists of a 2-by-2 matrix giving the auto-covariance of (x_i^p, x_i^p) and (y_i^p, y_i^p) on the diagonal axes and the cross-covariance (x_i^p, y_i^p) on the off-diagonal terms in the

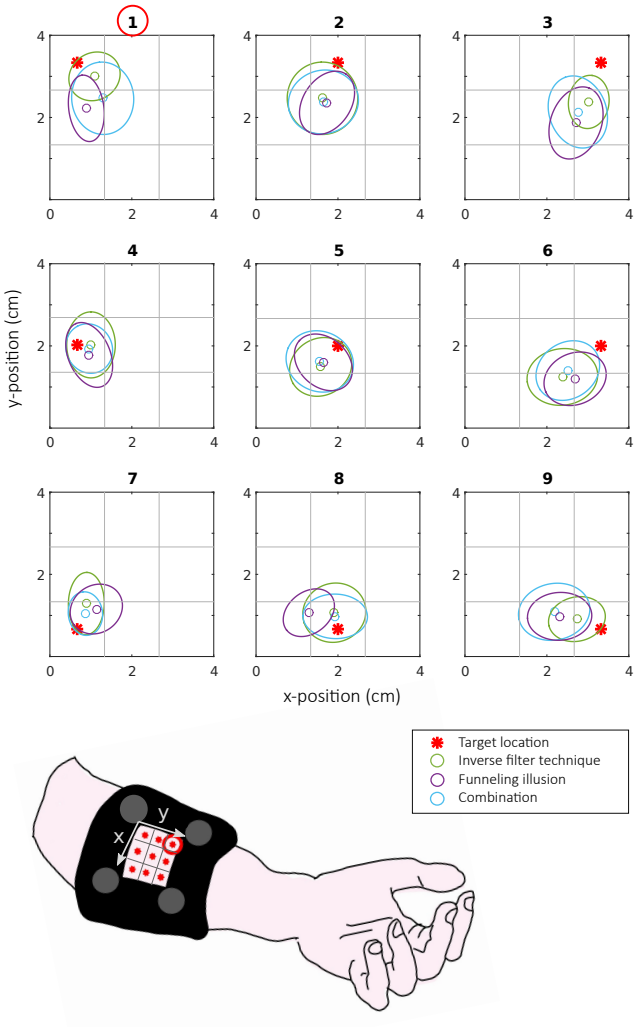

Fig. 8. Results of user study 1. Top: The results of the precision and accuracy for each rendering method per target location. The red stars are the target locations and the three other coloured circles show the mean position of the tactile sensation perceived by all participants. The ellipses around the mean show the accuracy of the perceived vibration. In the figure on top, a red circle is highlighted on target location 1, which resembles the red circle in the visualization of the set-up at the bottom of this figure.

matrix. The covariance matrix is plotted as an ellipse at one standard deviation centred around the mean. Where the mean represents the accuracy, the covariance is a measure to show the precision of the identification task.

A two-way repeated measures ANOVA was conducted that examined the effect of the type of location (IV) and the type of rendering method (IV) on the error between the target and the perceived vibration (DV). The error is calculated as the Euclidean distance:

$$e_{tot} = \sqrt{(x_i^p - x_i^t)^2 + (y_i^p - y_i^t)^2} \tag{10}$$

Per method and location, 60 Euclidean distances (3 repetitions $\times$ 20 participants) were obtained. Simple main effects analysis showed that the type of location did have a statistically significant effect on the error ($F_{6,360} = 15.888, p = 0.000$). This result can also be seen in Figure 8, where the lower-left corner (4, 5, 7 and 8) outperformed the other locations in the grid. Here the means of all the perceived vibrations are localized inside the targeted grid, whereas this observation does not hold for the other five locations.

Furthermore, simple main effects analysis showed that the rendering method also has a statistically significant effect on the error ($F_{2,115} = 4.487, p = 0.014$). A post-hoc analysis with a Bonferroni correction found that there was only a significant difference between the IFT - FI method ($p = 0.011$). From the figure, it can be seen that the overall error for the IFT is lower compared to the FI. This is especially due to the improved results obtained at locations 1 and 3 with the IFT compared to the FI.

Moreover, there was a statistically significant interaction between the effects of location and rendering method on the error ($F_{12,726} = 3.825, p = 0.000$). A post-hoc test with a Bonferroni correction verified the specific interaction between the three types of rendering methods on each target location. The test reported only a statistically significant difference for 3 out of the 9 locations. The results are listed on the left in Table II. We found that for all three locations, the effect was only significant between IFT - FI and the IFT - Combi method. For all the other six target locations (1 middle, 4 edges, and 1 corner), there was no statistically significant difference between the rendering methods. This implies that for the locations in the middle and edges, where we were able to generate different S values, overall no significant difference was perceived between the three rendering methods.

Lastly, when zooming in on the specific interaction between the nine different locations per specific rendering method, we learn from the right column in Table II that for each rendering method there was a statistically significant difference in the locations. When no difference would have been found between a rendering method and the locations, all nine locations would have been perceived at the same distance with respect to each target for that same rendering method. As this is not the case, we can say that each different rendering method creates perceived vibrations at other locations with respect to the target.

Location	Methods p-value	Method	Locations p-value
Location 1	$p < 0.002$	IFT	$p < 0.000$
Location 3	$p < 0.002$	FI	$p < 0.000$
Location 9	$p < 0.001$	Combination	$p < 0.000$

TABLE II
OVERVIEW OF THE SIGNIFICANT INTERACTION OF INDEPENDENT VARIABLES (IV): LOCATION AND RENDERING METHOD ON THE DEPENDENT VARIABLE (DV): ERROR e_{tot} OF A TWO-WAY REPEATED MEASURES ANOVA

2) User study 2 - confidence: User study 2 evaluated the confidence level that participants had per rendering method. We demonstrate that the level of confidence is, alongside precision and accuracy, a measure to evaluate the performance

of each rendering method. The results of user study 2 are presented in Figure 9. We found a clear decrease in the average selected grid points for the inverse filter technique. Furthermore, for the trials when the target was inside the perceived area, the average selected grid points is higher for all rendering methods compared to when we take into account all trials. A two-way repeated-measures ANOVA examined the effect of the target location (IV) and rendering method (IV) on the number of grid points selected (DV). Simple main effects analysis showed that the rendering method did have a statistically significant effect on the number of grid points selected ($F_{2,115} = 6.152, p = 0.003$). A post hoc analysis revealed that only IFT - FI differ statistically from each other ($p = 0.003$). Moreover, simple main effects analysis found that the location also had a statistical effect on the number of grid points selected ($F_{7,418} = 3.692, p = 0.001$), indicating that for the locations in the corners, the average of grid points selected was lower than for the locations in-between the actuators. However, the interaction effect was non-significant, ($F_{11,681} = 0.719, p = 0.728$). All in all, the results indicate that participants have more confidence in localizing vibrotactile stimuli when they are presented with the inverse filter technique.

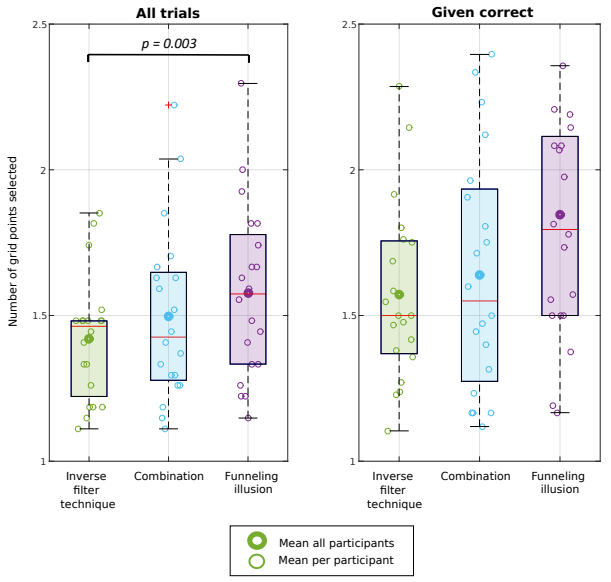

Fig. 9. Results of user study 2. The average number of grid points selected are plotted against the three different rendering methods in a boxplot. Left: represents the data from all trials. Right: shows only the data from the cases where the perceived grid area was located within the correct target.

VI. Discussion

In this study, three methodologies (inverse filter technique, funneling illusion, and a combination of the first two) were compared to generate perceptually localized vibration stimuli on the forearm where no physical actuators were present.

A. Surface Wave Propagation

Our skin vibration measurements showed that the inverse filter technique can create a desired focused wave (e.g., Ricker wavelet) onto a target location, while actively cancelling the displacement as much as possible at the remaining positions; see Figure 6a and 7a. Both figures demonstrated that all nine locations on the skin start displacing at different moments in time, all with different amplitudes and frequencies. Therefore, these results validate that through controlling the frequency, amplitude and phase of the driving signals the IFT manipulates the time of arrival of the waves at the target location. However, the aim of reaching zero displacement at the non-target locations was not achieved. This result could be caused by skin damping [31] and the small relative distance between the grid points. As each grid point is separated by 1.33 or 1.89 cm from the adjacent grid points and surface waves are very much damped throughout the distance they travel [2], the operation to achieve a maximum displacement at one location while cancelling it at the adjacent locations is a difficult one to achieve for the pseudo inverse operator.

Our results of the wave propagation of the funneling illusion revealed that no focused vibration was obtained at the virtual actuator; see Figure 6b and 7b. This is also consistent with the predictions from wave mechanics, namely that waves decay with the distance they travel from the stimulation point [16]. Furthermore, due to the frequency-dependent wave speeds, the waves did not arrive at the target at the same moment in time. These observations suggest that the waves originating from the stimulation point may interfere with each other at the target, however not in a constructive way such that the displacement amplitude at the target is higher than the displacement next to the actuators [32]. Hence, these results imply that the actual illusion is not caused by the constructive interference of travelling surface waves across the skin.

Moreover, from the middle column in Table I, we observed a difference between the type of location within the grid and the resulting signal strength values. Where signal strengths < 1 are obtained for when the middle and the edges were the target, this was not congruent for the locations at the corners. As the locations in the corners are the ones closest in contact with the physical actuators, it is logical that the surface wave departing from the nearby actuator will always be larger at the corners than the rest of the grid. This explains the positive signal strengths ($S > 1$) for all corners with the funneling illusion.

B. Perceptual Localization

The localization ability of the participants did not show significant differences with the three tested rendering techniques for the middle and edge grid locations. Interestingly, in those locations surface waves were successfully focused with the IFT. These results suggest that controlling the amplitude, frequency, and phase of a wave towards a target location has no direct influence on the human perceptual localization ability of vibrotactile stimuli on the arm.

Nonetheless, the localization ability of the participants was improved with the IFT for the majority of the corner locations, but not for all of them (see Fig. 8). We argue that the difference in the localization performance is due to the design of the wearable device. In our design, the inner diameter of the device was the same over the entire length. However, the diameter of the forearm is not constant and decreases as you move closer to the wrist. Accordingly, the two actuators next to locations 1 and 3 were not in full contact with the skin surface for most participants. Where the inverse filter technique does take this error into account in the calibration matrix $G(\omega)$, the funneling illusion does not. We claim that this is what makes the inverse filter technique perform better for locations 1 and 3 compared to the funneling illusion.

Furthermore, we found in user study 1 that for certain locations in the grid better localization results were obtained compared to other locations. This was the case for the grid points in the lower-left corner, namely locations 4, 5, 7 and 8. We suggest that the better localization results for all methods are due to a higher density of Pacinian Corpuscles in that specific region of the arm. However, as the density of this type of mechanoreceptor across the arm is yet unknown [33], further research should be conducted to verify this.

The results of user study 2 indicate that the overall confidence did improve with the inverse filter technique. This is an important conclusion as confidence is a measure of determination and assurance with which participants answered each trial. Therefore, we claim that the enhanced confidence is due to the focusing of the surface waves onto the skin.

The two user studies demonstrate that the overall ability to localize static stimuli on the forearm is low (compare mean perceived vibration location and target location in Figure 8). Earlier research by Cholewiak et al. [34] also supports these results. They compared the localization performance on the entire arm and found that the middle of the forearm is not a reliable source for static localization. They showed that localization improved towards the anatomical landmarks such as the wrist and elbow. It could be that for these locations the tactile density of mechanoreceptors is higher compared to the middle area of the volar forearm. Hence, localization performance with IFT may be improved for the body parts with a higher density of Pacinian Corpuscles, although this has not been investigated in this study.

C. Limitations and Future Work

The first limitation is associated with the limited amount of grid points we calibrated for. In total, we calibrated the skin on nine different points within a surface area of $4\times4\,cm^2$. Although we used a cubic interpolation function (see top row of Fig. 6 and 7) to evaluate how our skin moves at the locations between the nine calibrated grid points, the interpolation is based on assumptions and not on real-life data. For future research, we suggest taking more samples, especially at the locations next to the stimulation sites [17].

In our wearable device, the actuators are fully encapsulated into the 3D-printed casing, which makes it unfeasible to take displacement measurements from the actuators with the vibrometer. Therefore, our wave propagation plots are only represented by the nine grid points on the skin while displacement information on the actuators is lacking. This could have been mitigated by creating four small holes in the 3D-printed device at exactly the locations of the actuators.

During the calibration process participants had to hold their left arm fixed on the foam so that the vibrometer could measure the skin displacement at each grid point. Occasionally, participants accidentally moved their forearm during the calibration. In the future, these errors could be alleviated through the design of a holder in which the forearm of the participant would be fully stabilized [16].

In this paper, we defined confidence as the number of grid points selected, with nine being the maximum. However, when participants perceived a focused vibration at exactly the middle of multiple grid points, they were obliged to select all of these points. Although the vibration might have been felt as a focused one, the result illustrates a low confidence. Therefore, instead of having a grid of nine potential points, the participants could have drawn the perceived vibration in a grid with an infinitesimal amount of small grid points. This way, the obtained confidence is more accurate to what the participants perceived.

In the future, it would be interesting to test the rendering methods on other body parts with a higher density of mechanoreceptors, such as the palm or forehead [4]. Moreover, it would be advisable to use smaller actuators to make the device more wearable such that it corresponds to a more user-friendly experience.

D. Significance and Potential Applications

To the best of our knowledge, this is the first study that focused waves at the surface of the skin to create localized vibrotactile feedback. With the newly proposed rendering method, we conclude that we can constructively focus surface waves towards a target location on the arm where no physical actuator is present. Where the overall ability to pinpoint where in the grid the participants perceived the vibration signal was not improved with the inverse filter technique, confidence did improve significantly. Therefore, our findings can benefit industries interested in including localized vibrotactile feedback on the human body surface, such as the gaming, rehabilitation and sports industry.

REFERENCES

[1] A. Barghout, J. Cha, A. Saddik, J. Kammerl, and E. Steinbach, "Spatial resolution of vibrotactile perception on the human forearm when exploiting funneling illusion," in *2009 IEEE International Workshop on Haptic Audio visual Environments and Games*, 12 2009, pp. 19–23.

[2] K. Sofia and L. Jones, "Mechanical and psychophysical studies of surface wave propagation during vibrotactile stimulation," *IEEE Transactions on Haptics*, vol. 6, no. 3, pp. 320–329, 2013.

[3] L. A. Jones and N. B. Sarter, "Tactile displays: Guidance for their design and application," *Human Factors*, vol. 50, no. 1, pp. 90–111, 2008.

[4] G. Corniani and H. P. Saal, "Tactile innervation densities across the whole body," *REVIEW — Sensory Processing J Neurophysiol*, vol. 124, pp. 1229–1240, 2020. [Online]. Available: www.jn.org

[5] C. M. Reed, H. Z. Tan, Z. D. Perez, E. Courtenay Wilson, F. M. Severgnini, J. Jung, J. S. Martinez, Y. Jiao, A. Israr, F. Lau, K. Klumb, R. Turcott, and F. Abnousi, "A Phonemic-Based Tactile Display for Speech Communication," *IEEE Transactions on Haptics*, vol. 12, no. 1, pp. 2–17, 1 2019.

[6] J. B. F. Van Erp, H. A. H. C. Van Veen, C. J. Tno, H. Factors, and T. Dobbins, "Waypoint Navigation with a Vibrotactile Waist Belt," *ACM Transactions on Applied Perception*, vol. 2, no. 2, pp. 106–117, 2005.

[7] S. Choi and K. Kuchenbecker, "Vibrotactile display: Perception, technology, and applications," *Proceedings of the IEEE*, vol. 101, no. 9, pp. 2093–2104, 2013.

[8] A. Israr and I. Poupyrev, "Tactile Brush: Drawing on skin with a tactile grid display," in *Conference on Human Factors in Computing Systems - Proceedings*, 2011, pp. 2019–2028.

[9] T. G. Sato, M. Ohsuga, H. Boutani, and T. Moriya, "Tactile Phantom Sensation for Coaching Respiration Timing," *IEEE Transactions on Haptics*, vol. 8, no. 1, pp. 119–125, 1 2015.

[10] J. Salazar, K. Okabe, and Y. Hirata, "Path-Following Guidance Using Phantom Sensation Based Vibrotactile Cues Around the Wrist," *IEEE Robotics and Automation Letters*, vol. 3, no. 3, pp. 2485–2492, 7 2018.

[11] V. Hayward, "Tactile illusions," *Scholarpedia*, vol. 10, no. 3, pp. 1–19, 2015.

[12] G. von Bekesy, "Similarities Between Hearing And Skin Sensations," *The Psychological Review*, vol. 66, no. 1, pp. 1–22, 1959.

[13] S. Lederman and L. Jones, "Tactile and Haptic Illusions," *IEEE Transactions on Haptics*, vol. 4, no. 4, pp. 273–294, 2011.

[14] T. J. Moore, "A Survey of the Mechanical Characteristics of Skin and Tissue in Response to Vibratory Stimulation," *IEEE Transactions on man-machine systems*, vol. 11, no. 1, pp. 79–84, 1970.

[15] J. Andrews, M. Adams, and T. Montenegro-Johnson, "A universal scaling law of mammalian touch," *Science Advances*, vol. 6, no. 41, pp. 1–6, 2020. [Online]. Available: http://advances.sciencemag.org/

[16] B. Dandu, Y. Shao, A. Stanley, and Y. Visell, "Spatiotemporal Haptic Effects from a Single Actuator via Spectral Control of Cutaneous Wave Propagation," in *IEEE World Haptics Conference,*. Institute of Electrical and Electronics Engineers Inc., 7 2019, pp. 425–430.

[17] L. R. Manfredi, A. T. Baker, D. O. Elias, J. F. Dammann Ill, M. C. Zielinski, V. S. Polashock, and S. J. Bensmaia, "The effect of surface wave propagation on neural responses to vibration in primate glabrous skin," *PLoS ONE*, vol. 7, no. 2, pp. 1–10, 2 2012.

[18] Iheanacho F. and Vellipuram A.R., "Physiology, Mechanoreceptors," 1 2022.

[19] L. Jones, D. Held, and I. Hunter, "Surface waves and spatial localization in vibrotactile displays," in *IEEE Haptics Symposium*, 2010, pp. 91–94.

[20] C. Hudin and S. Panëels, "Localisation of Vibrotactile Stimuli with Spatio-Temporal Inverse Filtering," in *Haptics: Science, Technology, and Applications*. Cham: Springer International Publishing, 2018, pp. 338–350.

[21] L. Pantera and C. Hudin, "Multitouch Vibrotactile Feedback on a Tactile Screen by the Inverse Filter Technique: Vibration Amplitude and Spatial Resolution," *IEEE Transactions on Haptics*, vol. 13, no. 3, pp. 493–503, 7 2020.

[22] M. Tanter, J.-F. Aubry, J. Gerber, J.-L. Thomas, and M. Fink, "Optimal focusing by spatio-temporal inverse filter. I. Basic principles," *The Journal of the Acoustical Society of America*, vol. 110, no. 1, pp. 37–47, 2001.

[23] S. L. Gay and J. Benesty, *Acoustic Signal Processing for Telecommunication*, 2012, vol. 551.

[24] B. S. Masiero, J. Fels, and M. Vorländer, "Review of the crosstalk cancellation filter technique," *Proceedings of the International Conference on Spatial Audio*, pp. 112–116, 2011.

[25] C. Hudin and L. Pantera, "Sparse Actuator Array Combined with Inverse Filter for Multitouch Vibrotactile Stimulation," *2019 IEEE World Haptics Conference, WHC 2019*, pp. 19–24, 7 2019.

[26] D. Alles, "Information Transmission by Phantom Sensations," *IEEE Transactions on man-machine systems*, vol. 1, no. 11, pp. 85–91, 1970.

[27] J. Seo and S. Choi, "Initial study for creating linearly moving vibrotactile sensation on mobile device," in *IEEE Haptics Symposium*, 2010, pp. 67–70.

[28] G. Park and S. Choi, "Tactile information transmission by 2D stationary phantom sensations," in *Conference on Human Factors in Computing Systems - Proceedings*, vol. 256, 2018, pp. 1–12.

[29] J. C. Stevens' and K. K. Choo, "Spatial Acuity of the Body Surface over the Life Span," *Somatosensory & Motor Research*, vol. 13, no. 2, pp. 153–166, 1996.

[30] K. Barrett-Snyder, S. Lane, N. Lazarus, W. C. Kirkpatrick Alberts, and B. Hanrahan, "Printing a pacinian corpuscle: Modeling and performance," *Micromachines*, vol. 12, no. 5, 2021.

[31] C. Sherrick, "Variables affecting sensitivity of the human skin to mechanical vibration," *Journal of Experimental Psychology*, vol. 45, no. 5, pp. 273–282, 1953.

[32] I. Oakley, Y. Kim, J. Lee, and J. Ryu, "Determining the Feasibility of Forearm Mounted Vibrotactile Displays," *Proceedings - IEEE Virtual Reality*, pp. 27–34, 4 2006.

[33] V. A. Shah, M. Casadio, R. A. Scheidt, and L. A. Mrotek, "Spatial and temporal influences on discrimination of vibrotactile stimuli on the arm," *Experimental Brain Research*, vol. 237, no. 8, pp. 2075–2086, 8 2019.

[34] R. W. Cholewiak and A. A. Collins, "Vibrotactile localization on the arm: Effects of place, space, and age," *Perception and Psychophysics*, vol. 65, no. 7, pp. 1058–1077, 2003.

A

Wave Attenuation & Dispersion

In this chapter, we will explain how we retrieved the attenuation and dispersion numbers for any frequency between $50 - 500Hz$. These two variables form the basis for wave propagation on the skin.

A.0.1. Surface wave modelling

When our skin is stimulated by one vibration source, waves will propagate along the skin surface in all directions and into the tissue. These types of waves are called surface waves and can be modelled as harmonic plane waves. The formula for a harmonic plane wave is as follows:

$$\xi(\vec{x}, t) = e^{i(\vec{k}\vec{x} - \omega t)} \tag{A.1}$$

where $\xi(\vec{x}, t)$ is the time-varying displacement vector, $\vec{x}$ is position, t is time, $\vec{k}$ is the wave-number and ω the angular velocity. As our skin is viscoelastic, waves in such tissues are attenuated and dispersed, yielding frequency-dependent damping $\delta(f)$ and wave speeds $c(f)$. This implies that the formula for the harmonic plane wave needs to be extended, such that the wave number is a complex function, given by:

$$\vec{k} = k_1 + i\delta(f) \tag{A.2}$$

Here k_1 is the real part and given by $\frac{\omega}{c(f)}$, with $c(f)$ being the frequency-dependent wave speed. Furthermore, $\delta(f)$ is the imaginary part and represents the frequency-dependent damping coefficient. When we would plug this into equation A.1, this results in:

$$\xi(\vec{x}, t) = e^{i((\frac{\omega}{c(f)} + i\delta(f))\vec{x} - \omega t)} \tag{A.3}$$

This can be rewritten as follows:

$$\xi(\vec{x}, t) = e^{-\delta(f)\vec{x}} e^{i\omega(\frac{\vec{x}}{c(f)} - t)} \tag{A.4}$$

This formula describes an oscillating wave that decays exponentially with the distance travelled. Furthermore, the frequency of the driving signal of the vibrotactile actuator determines how quickly the wave will decay and the speed with which the wave will travel over the distance. Both the speed and the decay per frequency can be found using in-vivo Laser Doppler Vibrometer (LDV) measurements. This is explained in the next section.

A.0.2. Attenuation $\delta(f)$

We first analyzed the frequency-dependence of the spatial attenuation of vibrations on the arm via a vibrometer. See Figure A.1 for a visualization of the measurement set-up. A periodic frequency sweep sequence (chirp) from 50 to 500 Hz was sent to the actuator that was placed on the left volar side of the forearm. The vibrometer measured the displacement of skin motion normal to the forearm surface at 10 points that were equally distributed on a line from the actuator, each point 2.5 mm spaced from the

other. For each scanned measurement point, the forearm was presented with the chirp via the actuator, while displacement data was collected at the measurement point. Next, both the driving signal and the measured displacement at a measured point were transformed to the Fourier domain and divided by each other, which yields a transfer function between one measurement point and the actuator. Eventually, 10 transfer functions are obtained, one for each measurement location.

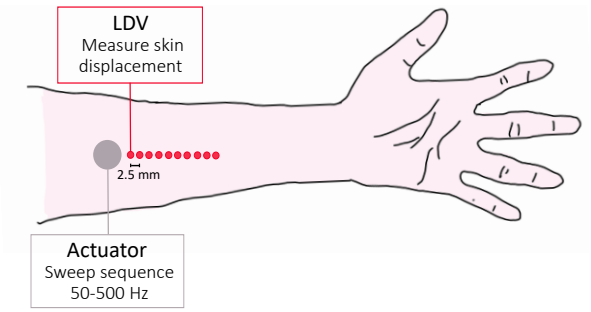

Figure A.1: Measurement set-up to obtain the frequency dependent attenuation & dispersion relationship

Now that the transfer functions are known, the attenuation coefficient for any frequency between 50-500 Hz can be retrieved. This was done as follows. For one frequency component, we could plot the corresponding absolute values of the 10 transfer functions against the 10 distances on the horizontal axis. This results in an exponentially decaying function. In MATLAB, we fitted a curve over the measured data points with the following characteristics:

$$y = e^{-\delta x} \tag{A.5}$$

Here δ is the damping coefficient. Eventually, this was repeated for all frequencies, such that for each frequency we obtained a separate δ. The attenuation relation per frequency can be seen at the top of Figure A.2. From analyzing the figure, it is clear that a vibration at the forearm decays with the distance travelled from the stimulation point in a frequency-dependent manner. The higher the damping coefficient the faster a wave attenuates. From the data, we learn that the high frequency stimuli $(f = 500Hz)$ decay more rapidly over distance than the low frequency stimuli $(f = 50Hz)$. Although, from $250Hz$ the curve already plateaus. These results are in accordance with previous research [1].

A.0.3. Dispersion $c(f)$

From equation A.4, we learned that the speed of the wave $c(f)$ is also frequency dependent. The speed can be calculated as follows:

$$c(f) = \frac{\omega}{k} \tag{A.6}$$

Here k represents the wave number and is defined as the number of wavelengths per unit distance in $\frac{rad}{m}$. Moreover, ω is the angular frequency and given by $2\pi f$ in $\frac{rad}{s}$. For each frequency component, we could calculate the wave number in order to obtain the corresponding wave speed. This was done as follows. We plotted the phase change of the 10 different transfer functions over the distance travelled for a given frequency signal. This resulted in a linear graph with on the y-axis the phase in rad and the distance travelled in m over the x-axis. Then, we fitted a linear function over the measured data such that the slope of the linear fit represents the wave number k for one frequency component. Next, k could be inserted into equation A.6 to obtain the corresponding wave speed for the given frequency. Eventually, this was repeated for all frequencies, such that for each frequency we found a unique wave speed c. The dispersion relation per frequency can be seen at the bottom of Figure A.2. From the figure, it is clear that from $150Hz$ on-wards, the speed increases with a constant rate. This implies that the higher frequencies travel faster than the lower frequencies. For the frequencies between $50 - 125Hz$, a constant speed was found of $4m/s$. To conclude, from the aforementioned experiment we found

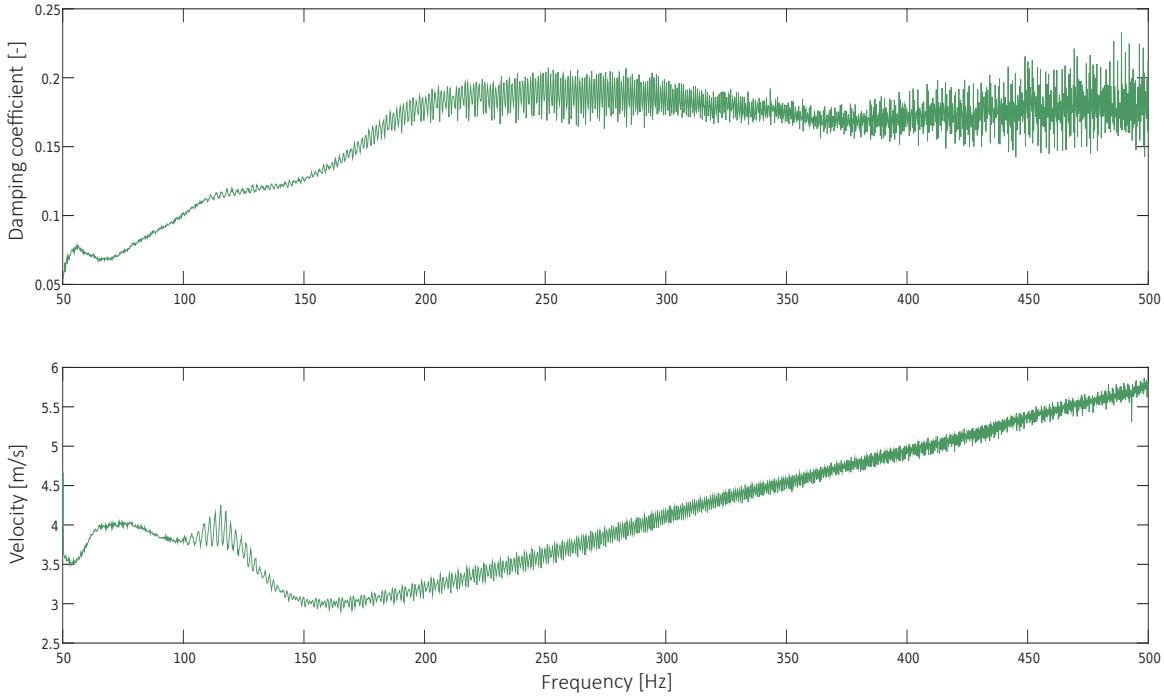

Figure A.2: Frequency-dependent wave attenuation & dispersion relationship

that the low-frequency stimuli excite waves that extend further from the excitation point and travel with slower speeds than the high-frequency stimuli.

Bibliography

[1] B. Dandu et al. “Spatiotemporal Haptic Effects from a Single Actuator via Spectral Control of Cutaneous Wave Propagation”. In: *IEEE World Haptics Conference,* Institute of Electrical and Electronics Engineers Inc., July 2019, pp. 425–430. ISBN: 9781538694619. DOI: 10.1109/WHC.2019.8816149.